2001-2481

THE EFFECT OF RIDGE-ICE LOCATION AND THE ROLE OF AIRFOIL GEOMETRY

Sam Lee* and Michael B. Bragg+
University of Illinois at Urbana-Champaign, Urbana, IL 61801

ABSTRACT

The findings from a recent University of Illinois investigation on the effect of ridge ice location on airfoil aerodynamics using additional airfoils are presented. Previous studies involving two airfoils (NACA 23012m and NLF 0414) showed that the most severe performance penalties were observed when the simulated ridge ice was located near the adverse pressure recovery region of the clean model. Two more airfoils (a commuter aircraft wing and tail sections) were tested and original findings were confirmed. The results from the commuter airfoils showed that an airfoil's sensitivity to SLD ice accretion (ridge ice that typically form between 10-20% chord) was dependent largely on its load distribution. If the airfoil was more front-loaded, then its performance degradation due to SLD ice accretion tended to be more severe.

NOMENCLATURE

C_d	Drag coefficient
C_h	Flap hinge-moment coefficient
C_l	Lift coefficient
$C_{l,max}$	Maximum lift coefficient
C_m	Pitching-moment coefficient
C_p	Pressure coefficient
$C_{p,min}$	Minimum pressure coefficient
M	Mach number
Re	Reynolds number
c	Model chord length
k	Protuberance height
t	Airfoil thickness
x	Model coordinate in chordwise direction
α	Angle of attack

INTRODUCTION

The "critical ice accretion" is usually described as the one ice formation that causes the maximum degradation in aircraft performance and control. However, accurately determining a critical ice accretion for an aircraft is difficult because the effects of a particular ice accretion on aircraft aerodynamics are dependent on several factors: the ice-accretion geometry, size and location, the airfoil geometry, aircraft 3-D configuration, the flight Reynolds number, Mach number, etc.

Past studies have shown that, generally, the larger ice shape sizes resulted in more severe performance and control degradations.[1,2,3] The more streamlined ice shape geometries also resulted in less performance and control degradation.[1,3] Also, iced-airfoil aerodynamics was shown to be relatively insensitive to Reynolds number variations[4,5,6] Lee, Kim, and Bragg[7] provided a comprehensive review of the effects of some of the parameters described above.

Recent studies at the University of Illinois at Urbana-Champaign (Illinois)[1,7,8] with spanwise ridge ice (typically found in SLD encounters) have shown that airfoil aerodynamics are particularly sensitive to the ice-shape location. However, significant differences were observed on the two airfoils tested, the NACA 23012m and the NLF 0414. The effects of the simulated ice shapes were much more severe on the NACA 23012m, with a $C_{l,max}$ as low as 0.25 for the ice shape with a k/c = 0.0139. The lowest true $C_{l,max}$ measured for the NLF 0414 with same ice shape was 0.68. This was attributed to the large differences in the clean-model surface pressure distribution of these two airfoils.

Because the two airfoils tested were so different, it was difficult to conclude precisely what aerodynamic characteristics of the clean airfoil were important in

* Graduate Research Assistant, Department of Aeronautical and Astronautical Engineering, Student Member AIAA
+ Professor and Head, Department of Aeronautical and Astronautical Engineering, Associate Fellow AIAA

determining its sensitivity to ice-shape location. In order to answer this question, two additional airfoils were tested at Illinois with spanwise ridge ice at various chordwise locations. The purpose of the current paper is to incorporate the results of this test with the results of the previous Illinois tests[1,7] in order to provide a more complete picture of the effects the airfoil geometry in determining its sensitivity to the ice-accretion location.

EXPERIMENTAL SETUP

All of the tests described in this report were performed in the University of Illinois 3'x4' Subsonic Wind Tunnel. Four 18-inch chord airfoil models were used: a modified NACA 23012m model (described in more detail in Lee, et al.[9]), a NLF 0414 model, and a wing and tail airfoil models from a commuter aircraft currently in service. The wing airfoil was a modified NACA 63A415, and the tail airfoil was a modified NACA 63A213. A 25% chord simple flap was present on the NACA 23012m and NLF 0414 models. The two commuter models did not have flaps.

Figure 1 is a schematic of the experimental setup. The model was attached to a three-component balance, which was also used to set the angle of attack. A load cell on the flap actuation linkage measured the flap-hinge moment on the flapped models. All of the models had surface pressure taps in order to measure the pressure distribution. A traverseable wake rake with 59 total-pressure probes was used to measure the wake pressures, from which the drag was determined. The pressures were measured using an electronically scanned pressure (ESP) system.

The lift coefficient (C_l) and pitching moment coefficient (C_m) measurements were derived from both the force balance and the surface pressure measurements. The drag coefficient (C_d) measurements were taken with the wake rake. The flap-hinge-moment coefficients (C_h) on the NACA 23012m and NLF 0414 models were measured with the flap-hinge load cell and confirmed with the surface pressure measurements. For the commuter models (which did not have flaps), the hinge moment was obtained by integrating the surface pressure over an imaginary flap located between x/c = 0.75 and the trailing edge. The C_l, C_m, and C_d measurements were calculated using standard methods with conventional definitions. The C_h was obtained by determining the trailing-edge-down moment about the flap-hinge line and nondimensionalizing by the flap surface area and the flap chord length. All of the aerodynamic coefficients were corrected for wall effects using the method described by Rae and Pope.[10]

The ridge-ice shapes were simulated with wooden forward-facing quarter-round shapes of k = 0.25" (k/c = 0.0139) as shown in Fig. 2. The boundary layer was tripped at x/c = 0.02 on the upper surface and at x/c = 0.05 on the lower surface using 0.012-inch diameter microbeads. All of the tests were conducted at Re = 1.8 million and M = 0.18.

RESULTS AND DISCUSSION

Included in this section is the analysis of the effect of the ridge-ice location on the four airfoils tested at Illinois. Some of the results from the NACA 23012m and NLF 0414 have been published previously.[1,7] However, they are presented here again for comparisons to the results from the commuter wing and tail airfoils, which have not been previously published

Figure 3 shows the comparison of the geometry of the four airfoils tested. The airfoils were grouped in pairs that had similar geometries (and aerodynamic characteristics). The commuter wing was the thickest airfoil tested (t/c = 0.16). The commuter tail was the thinnest airfoil (t/c = 0.11). The commuter wing and NLF 0414 were highly cambered while the NACA 23012m and commuter tail were not. It is interesting to note that first 30% chord of the NLF 0414 and the commuter tail airfoils were very similar.

Clean Model Pressure Distribution

Figure 4 shows the clean-model pressure distribution comparison at a nominal lift coefficient of 0.5. Because of varying degree of camber, each model was at a different angle of attack.

The NACA 23012m has a very large suction peak (with $C_{p,min}$ = -1.4) centered near x/c = 0.08. There was a severe pressure recovery (with very adverse pressure gradient) from x/c = 0.08 to 0.22. The pressure recovery became more gradual downstream of this location and extended to the trailing edge.

The commuter wing airfoil had a pressure distribution that was quite different. A large suction peak was not present on this airfoil at this angle of attack, with a $C_{p,min}$ value of only -0.93 located at x/c = 0.23. Because a large suction peak was not present, the pressure recovery was very gradual, with a nearly constant pressure gradient extending from x/c = 0.25 to 0.80. The pressure gradient became more adverse between x/c = 0.80 and the trailing edge.

The NLF 0414 had a nearly constant C_p between x/c = 0.04 to 0.72. The pressure recovery did not start until x/c = 0.72. Because of the short recovery region, the adverse pressure gradient in this region was the most severe of the four airfoils tested.

The commuter tail airfoil was similar to the NLF 0414 in that the C_p was relatively constant (with a slight adverse gradient) between x/c = 0.03 and 0.45, with most of the recovery occurring between x/c = 0.45 and the trailing edge. Because the pressure recovery region on the commuter tail was larger than on the NLF 0414, the adverse pressure gradient was not as severe.

Integrated Coefficients

Figures 5 shows the lift coefficient on the four models with the simulated ridge ice located at x/c = 0.02, 0.10, and 0.20. Figure 5a shows that varying the ridge-ice location in this range on the NACA 23012m had a significant effect on the lift coefficient. When the ridge ice was located at x/c = 0.02, there was a clearly defined $C_{l,max}$ of 0.53 at $\alpha = 7°$. When the ridge ice was located at x/c = 0.10, a clearly defined $C_{l,max}$ was not present. Instead, the lift coefficient plateaued at $\alpha = 3°$ and remained nearly constant to $\alpha = 9°$. The highest lift coefficient value obtained was 0.27. When the ice ridge was located at x/c = 0.20, a $C_{l,max}$ in the traditional sense was not present. There was a break in the lift curve slope at $\alpha = 2°$, after which lift increased linearly with angle of attack, but at a much reduced rate when compared to the clean model. Flow visualization had shown that the airfoil was separated soon after the break in the slope.

Figure 5b show the effect of ridge-ice location on the commuter wing airfoil. It shows that unlike the NACA 23012m, there was a clearly defined $C_{l,max}$ at all three ice-ridge locations. When the ice shape was located at x/c = 0.02, the $C_{l,max}$ was 0.82. The $C_{l,max}$ value dropped to 0.56 and 0.33 when the ridge ice was located at x/c = 0.10 and 0.20. The angle of attack at which the model stalled decreased from 8° to 4° as the ice shape location was moved downstream from x/c = 0.02 to 0.20.

Varying the ridge ice location between x/c = 0.02 and 0.20 had very little effect on the NLF 0414, as Fig. 5c shows. When the ridge ice was located at x/c = 0.02, the $C_{l,max}$ was 0.74. The $C_{l,max}$ only changed to 0.71 when the ice ridge was located at x/c = 0.20. The lift curves for the three iced cases were very similar as well.

The effect of ridge-ice location on the commuter tail airfoil is shown on Fig. 5d. $C_{l,max}$ was present for these iced cases but was not as clearly defined as on the NLF 0414. After a break in the lift curve slope, the C_l reached a plateau and did not vary significantly with angle of attack. There was a slight variation in the $C_{l,max}$ with the ice-ridge location, but was not as large as observed on the NACA 23012m and the commuter wing airfoil. When the ice ridge was located at x/c = 0.02, the $C_{l,max}$ was 0.70. When the ridge ice was located at x/c = 0.20, this reduced to 0.58.

Figures 6 shows the drag polars of the four models with the simulated ridge ice located at x/c = 0.02, 0.10, and 0.20. Figure 6a shows the drag polars on the NACA 23012m. Location of the simulated ice shape had a significant effect on drag. The lowest drag was observed when the simulated ice shape was located at x/c = 0.02. Significantly higher drag was observed then the simulated ice ridge was located at $x/c = 0.10$ and 0.20. The drag ploars at these two ice-ridge locations appeared very similar. However, at $C_l < 0$, the x/c = 0.20 had slightly higher drag. At $C_l > 0$, the x/c = 0.10 case had higher drag. This corresponded well to the lift values shown on Fig. 5a, which showed that x/c = 0.02 case had the highest lift, followed by x/c = 0.20, and x/c = 0.10

Figure 6b show the effect of ridge-ice location on the commuter wing airfoil. It shows that as the ridge ice location was increased from x/c = 0.02 to 0.20, the drag increased as well. Figure 6c shows the drag polars on the NLF 0414. It also shows that as the ridge-ice location was varied between x/c = 0.02 to 0.20, the drag increased as well. There was significant variation in the drag polars even though the lift curves (Fig. 5c) were very similar. Figure 6d shows the drag polars on the commuter tail. Again, as the ice ridge was moved downstream from x/c = 0.02 to 0.20, the drag increased.

Figure 7 shows the effect of the ridge-ice location the pitching moment. Pitching moment is a good indicator of the onset of rapid bubble growth since it is a measure of load distribution. The onset of rapid bubble growth is usually indicated by a negative break in the pitching moment curve as the growing bubble starts to induce a strong nose-down pitching moment. Figure 7a shows the effect of ridge-ice location on the NACA 23012m. When the ridge ice was located at x/c = 0.02, the break in the pitching moment occurred at $\alpha = 5$. When the ridge ice was located at x/c = 0.10 and x/c = 0.20, the break in C_m occurred at $\alpha = -1°$ and $\alpha = -4°$, respectively.

Similar results were observed for the other three airfoils tested, as Figs. 7b to 7d show. Figure 7b shows that on the commuter wing, the angle of attack at which break in the C_m curve occurred decreased form 8° to 0° as the ice-ridge location was varied from x/c = 0.02 to 0.20. On the NLF 0414, the angle of attack decreased from 5° to 4°, while on the commuter tail, the angle of attack decreased from 6° to 0°.

It is interesting to note that the least amount of variation in the angle of attack at which the C_m broke was observed on the NLF 0414, followed by the commuter tail. These also happened to be the two airfoils with the least amount of variation in lift as the

ice ridge location was varied. Also of interest was that as the ridge ice was moved further downstream from the leading edge, the break in the pitching moment became more gradual and the magnitude of the $C_{m,\alpha}$ value decreased.

Figure 8 shows the effect of ridge-ice location on the flap-hinge moment. Flap hinge moment usually serves as a good indicator of when the separation bubble reaches the flap. When the bubble reaches the flap, a strong flap nose-down pitching moment is generated, creating a sharp negative break in the C_h curve. This break in the C_h curve usually occured a few degrees angle of attack after the break in the C_m curve.

Figure 8a shows the hinge moment on the NACA 23012m. When the ridge ice was located at x/c = 0.02 the break in the hinge moment occurred at $\alpha = 6°$. When the ridge ice was located at x/c = 0.10 and x/c = 0.20, the break in C_h occurred at $\alpha = 1°$ and $\alpha = 0°$, respectively.

Similar results were observed for the commuter wing and tail airfoils. On the commuter wing, the angle of attack at which the break in C_h occurred decreased from $\alpha = 7°$ to $\alpha = 1°$ when the ridge-ice location was varied from x/c = 0.02 to 0.20. On the commuter tail, the angle of attack at which the break in C_h occurred decreased from $\alpha = 6°$ to $\alpha = 3°$ when the ridge-ice location was varied from x/c = 0.02 to 0.20.

The hinge moment on the NLF 0414 behaved quite differently from the other three airfoils, as Fig. 8c shows. The iced hinge moments were similar to the clean values at nearly all angles of attack. This was due to trailing-edge separation that was present on the clean model. Because the trailing edge (and significant portion of the flap) was already separated when the bubble reached the flap, there was not a large change in the C_h value. Because of this, the flap hinge moment did not yield results of any interest.

Figure 9 shows a summary of $C_{l,max}$ as a function of the ridge-ice location for the four airfoils tested. Figure 5 to 8 showed the results from only three ridge-ice locations. However, the ridge ice was tested at many more locations in order to accurately determine the most critical chordwise location for these four airfoils. Figure 9 provides a summary of the cases tested. All the models were tested with ice shapes located as far downstream as mid-chord. However, only the data points for which a clear $C_{l,max}$ existed are shown. For example, on the NACA 23012m, a $C_{l,max}$ in the traditional sense was not observed when the ridge ice was located between x/c = 0.14 and 0.30. Figure 9 shows that, generally, moving the ridge ice downstream resulted in larger degradations of maximum lift. For all four airfoil models, the highest $C_{l,max}$ was observed when the ridge ice was located at the leading edge. The NACA 23012m was most sensitive to the ridge ice location in the first 15% chord. This was followed by, the commuter wing, the commuter tail, and the NLF 0414. There was little variation in $C_{l,max}$ when the ridge-ice location was varied between x/c = 0.02 and 0.20 on the NLF 0414 and the commuter tail. However, on the NACA 23012m and the commuter wing, moving the ridge-ice from x/c = 0.02 to 0.20 caused significant reductions in the maximum list.

Figures 10 to 13 show the effect of the ridge ice location on the changes in the integrated coefficients from the clean model. Figure 10 shows the ΔC_l ($C_{l,clean} - C_{l,iced}$), or the lift loss compared to the clean airfoil, due to the simulated ridge ice. Each curve represents a fixed angle of attack, and the simulated ice shape location is depicted on the x-axis. Also shown on the figure by the solid arrows are the locations of maximum local air velocity or $C_{p,min}$ (of the clean airfoil) for each angle of attack and by the open arrows are the location of the maximum adverse pressure gradient (also of the clean airfoil). Figure 10a shows that on the NACA 23012m, ΔC_l remained relatively small and did not vary significantly with the ice shape location at angle of attack of 0°. The ΔC_l values remained approximately at 0.04 at all x/c locations except at the leading edge where it was nearly zero. Increasing angle of attack increased the lift loss at all ice shape locations. The largest lift loss occurred when the ice shape was located at x/c = 0.12 and did not change with angle of attack until $\alpha = 9°$ where it moved upstream to x/c = 0.10. The simulated ice-shape location for maximum lift loss was well downstream of the maximum local air velocity and slightly upstream of the maximum adverse pressure gradient. The x/c = 0.12 ice-ridge location was near the same x/c location that produced the lowest $C_{l,max}$ as shown in Fig. 9.

Figure 10b shows the lift loss on the commuter tail. The maximum adverse gradient location was not shown for $\alpha \leq 6°$ because it was near the trailing edge and outside of the x-axis range shown on the plot. For $\alpha = 9°$ (where the maximum adverse gradient is shown), the ridge-ice location with the largest lift loss appeared to coincide with the location of the maximum adverse pressure gradient.

Figure 10c shows the lift loss ΔC_l on the NLF 0414. When the ice shape was placed between x/c = 0.02 and 0.20, there was not a large variation in the lift loss. This was similar to what was observed in the $C_{l,max}$ plot of Fig. 9. It was only when the ice shape was located downstream of x/c = 0.30, and closer to the adverse pressure gradient at the trailing-edge pressure recovery that a much larger increase in the lift loss was observed. This was even the case at $\alpha \geq 3°$ where the adverse pressure gradient associated with the leading-

edge suction peak was more severe than the trailing-edge pressure recovery.

Fig. 10d shows the lift loss on the commuter tail. It shows that the lift loss was relatively insensitive to the ridge-ice location (except at the leading edge) at all angles of attack shown. This behavior was similar to that observed on the NLF 0414, but for a much larger range of chordwise location. However, because the ridge ice was not tested downstream of x/c = 0.40, it is not known for how much of the chord this behavior would have existed.

Figure 11 shows the change in drag ΔC_d ($C_{d,clean} - C_{d,iced}$) compared to the clean airfoil due to the 0.25" ice shape simulation. Again solid arrows show the location of the maximum local air velocity and the open arrows show the location of the maximum adverse pressure gradient. Figure 11a shows that on the NACA 23012m, there was significant variation ΔC_d with the ice shape location even at angles of attack as low as 0°. At this angle of attack, the largest increase in the drag was observed when the ice shape was located at x/c = 0.12. As the angle of attack was increased, ΔC_d increased as well. However, as the angle of attack was increased, the ice shape location where the largest drag increase occurred moved upstream as well. At α = 3°, this occurred at x/c = 0.10 and at α = 9°, this occurred at x/c = 0.02. The most critical location in terms of drag increase appeared to coincide with the location of maximum local air velocity.

Figure 11b shows the drag change on the commuter wing. Unlike on the NACA 20312m, the ridge-ice location with the largest drag increase did not correspond to the location of the largest local air velocity. At α = 3°, the largest drag increase occurred when the ridge ice was located at x/c = 0.30. However, the location of the maximum local air velocity was 0.17. The maximum drag increase location did not coincide with the location of the maximum adverse gradient either. However, it was located between the location of maximum local air velocity and the maximum adverse gradient.

Figure 11c shows the drag change on the NLF 0414. At α = 0° and 3°, the largest change in drag occurred when the ridge ice was located near x/c = 0.4. At higher angles of attack (α = 6° and 9°) the most critical ridge ice location moved upstream towards the leading edge. Neither maximum local air velocity nor adverse pressure gradient was an indicator of the most critical ridge ice location in terms of changes in drag. As with lift, there was little change in ΔC_d when the ridge ice location was varied between x/c = 0.02 and 0.20.

Figure 11d shows the drag change on the commuter tail. The results were similar to that of the NLF 0414. At lower angles of attack (α = 0° and 3°) the most critical ridge-ice location was near x/c = 0.40. However, at the highest angle attack shown (α = 9°), the most critical location was near the leading edge. Neither maximum local air velocity nor adverse pressure gradient was an indicator of the most critical ridge ice location in terms of drag change.

Figure 12 shows ΔC_m ($C_{m,clean} - C_{m,iced}$), the change in the pitching moment due to the ridge ice simulation. Figure 12a shows the pitching moment change on the NACA 23012m. At α = 0°, the ice shape did not have any effect on C_m when it was located at the leading edge. As it was moved downstream, the ΔC_m became more negative, which indicated that the pitching moment became more nose up than the clean case. However, at x/c = 0.04, ΔC_m started to increase, reaching a value of 0.02 when the ridge ice was located at x/c = 0.12, after which it leveled off. As the angle of attack was increased, the x/c location at which the ΔC_m started to increase moved upstream. The location where the ΔC_m peaked also moved upstream with angle of attack and appeared to coincide with the location of the maximum local air velocity.

Similar results were observed for the commuter wing, as Fig. 12b shows. However, the location at which the peak ΔC_m values were observed did not coincide with the location of the maximum local air velocity (but was further downstream). Figure 12c shows the changes in the pitching moment for the NLF 0414. As with lift and drag, the location of the maximum change in C_m was located near x/c = 0.40 for low angles of attack (α = 0° and 3°) and near the leading edge for high angle of attack (α = 9°). Figure 12d shows the pitching moment change on the commuter tail airfoil. The results again were similar to that of the NLF 0414.

Figure 13 shows the effect of the simulated ridge ice on ΔC_h ($C_{h,clean} - C_{h,iced}$). The results were very similar to that of ΔC_m shown in Fig. 12. Figure 13a shows the change in the hinge moment on the NACA 23012m. At α = 0°, the ice shape did not have any effect on C_h when it was located at the leading edge. As it was moved downstream, the ΔC_h became more negative, which indicated that the hinge moment became more nose up than the clean case. However, at x/c = 0.12, ΔC_h value leveled off and remained nearly constant until x/c = 0.30. At α = 3°, the ΔC_h value reached a peak (or a maxima) at x/c = 0.12. The location where the ΔC_h peak occurred moved upstream with increasing angle of attack. Largest changes in C_h were observed when the simulated ice shapes were located between the locations of the maximum local air velocity and the maximum adverse pressure gradient.

Figure 13b shows the changes in the flap hinge moment on the commuter wing airfoil. The trends were similar to that of the NACA 23012m. However, the location of the maximum local air velocity coincided with the onset of the rapid rise in ΔC_h. Figure 13d shows the change in flap hinge moment on the commuter tail. Again, the trends were similar to that of the NACA 23012m and the commuter wing. However, the location of the maximum local air velocity was not an indicator of the onset of rapid rise in ΔC_h.

The results of Figs. 10 to 13 showed that critical ridge-ice location where the maximum changes in C_l, C_d, C_m, and C_h occurred were generally related to the location of the maximum local air velocity and the maximum adverse pressure gradient. However, precise relationship depended greatly on the particular integrated aerodynamic coefficient and the airfoil geometry.

Flowfield Analysis

The reason for the differences in the sensitivity of the airfoils to the ridge-ice location was attributed to the differences in the clean-model pressure distributions (Fig. 4). Generally, the severity of the effect of ridge ice is directly related to the length of the separation bubble that forms downstream of the ice shape. This in turn is determined primarily by the severity of the adverse pressure gradient downstream of the ice shape, over which the bubble is forced to reattach. More severe adverse gradient typically results in longer separation bubble. The effect of ridge ice on surface pressure distribution is shown on Fig. 14. All of the clean models are at $C_l = 0.5$, which explains the various angles of attack. Before the iced-airfoil pressure distribution is discussed, it is important to understand the basic features. Figure 14b shows pressure distribution on the commuter wing airfoil with the ridge ice at x/c = 0.10. On the upper surface, the C_p decreased as the flow initially accelerated from the leading edge to x/c = 0.06, where it started to decelerate as it encountered an adverse pressure gradient due to the ridge ice. The flow then accelerated again over the ridge ice and separated, resulting in a region of relatively constant C_p between x/c = 0.10 and 0.22. The C_p then increased as the reattachment process began. The reattachment occurred where the iced C_p value approached the clean value and started to take on similar form, at x/c = 0.35. A more complete description of the iced-airfoil pressure distribution can be found in Lee and Bragg.[1,8]

Figure 14a shows why the NACA 23012m was the most sensitive airfoil when the ridge ice was located in the first 20% chord. Because the NACA 23012m had a large suction peak near the leading edge, it also had a very severe pressure recovery region that extended from x/c = 0.10 to 0.20. If an ice shape was located upstream of x/c = 0.20, the resulting separation bubble would be located in this region of very adverse pressure gradient. The bubble cannot easily reattach in this region, resulting in a long bubble. This is shown on Fig. 14a, where the ridge ice was located at x/c = 0.10. The pressure distribution on the upper surface of the iced airfoil did not approach the clean case after the initial separation over the ice shape. This indicated that the bubble failed to reattach on the airfoil.

The adverse gradient on the commuter wing was not as severe as the NACA 23012m. Thus, the separation bubble that formed downstream of the ice shapes was not as large, resulting in less lift degradation. This is shown on Fig. 14b. The bubble appeared to have reattached at x/c = 0.35.

The pressure gradient on the NLF 0414 is shown on Fig. 14c. On the clean model, the adverse gradient (where the recovery took place) on the NLF 0414 did not begin until x/c = 0.74. Ahead of the recovery region, the pressure gradient was nearly zero. Because of this, the lift was relatively insensitive to the ice shape location, as the bubble did not encounter an adverse pressure gradient. It was not until the ridge ice was located at x/c = 0.30 that the bubble encountered the adverse gradient and the maximum lift started to decrease. When the ridge ice was located at x/c = 0.10, the bubble reattached at x/c = 0.35.

The commuter tail airfoil was similar to the NLF 0414 in that there was a region of nearly constant surface pressure extending from the leading edge, as shown on Fig. 14d. However, this extended to only x/c = 0.45. Most of the pressure recovery occurred downstream of x/c = 0.45 where there was a more severe adverse gradient. When the ridge ice was located at x/c = 0.10, the bubble reattached at x/c = 0.40. Figure 9 shows that the commuter tail was slightly more sensitive to the ridge-location than the NLF 0414 because of the slight adverse pressure gradient present between x/c = 0.03 and 0.45. However, it was less sensitive than either the NACA 23012m or commuter wing airfoil due to the region of nearly constant pressure.

The results shown above indicated that generally the more front loaded the airfoil was (with large leading-edge suction peak), the more sensitive it was to SLD-type ridge ice accretion. Of the four airfoils tested, the NACA 23012 was the most front-loaded, with the largest suction peak. It had the largest performance degradation due to ridge-ice accretion, especially in the 10-20% chord range where it is likely to occur. The NLF 0414, which was the most aft-loaded of the airfoils tested, was the most insensitive to

SLD ridge ice accretion. The two commuter airfoils fall in between the NACA 23012m and NLF 0414 in terms of their front-loadedness. The performance degradations on the commuter airfoils, thus, fall in between the NACA 23012m and NLF 0414.

SUMMARY

Recent studies at Illinois have shown that airfoil geometry was an important factor in determining a particular airfoil's sensitivity to ice-shape location. Because only two airfoils (the NACA 23012m and the NLF 0414) were used in these investigations, it was difficult to conclude exactly what the important features were in determining an airfoil's sensitivity to ridge-ice location. Thus, two additional airfoils (commuter aircraft wing and tail) were tested with ridge ice at various chordwise locations. These results were then compared to the NACA 23012m and the NLF 0414.

The results from the two commuter airfoils confirmed that the largest losses in lift occurred when the ridge ice was located near the region of the adverse pressure gradient of the clean model, where the pressure recovery occurred. The exact location, however, varied with different airfoils tested. On the NACA 23012 and commuter wing, the most critical location was the region between the location of the maximum local air velocity and the maximum adverse pressure gradient. On the NLF 0414 and the commuter tail, the most critical location was the trailing edge pressure recovery region.

The findings also showed that an airfoil's sensitivity to SLD ridge ice accretion (which usually forms between 10-20% chord) was largely dependent on it's the load distribution. The airfoil that was very front-loaded, with large leading-edge suction, tended to have the most severe performance degradation due to SLD-type ice accretion. In contrast, the most aft loaded airfoil with favorable or zero pressure gradient near the leading edge was the least sensitive to SLD-type ice accretion.

.

ACKNOWLEDGEMENTS

This work was primarily supported by the Federal Aviation Administration (FAA) under grant DTFA MB 96-6-023 The authors would like to thank Systems Technology, Inc. for the commuter airfoil models used in this study.

REFERENCES

[1] Lee, S. and Bragg, M. B., "Effects of Simulated Spanwise-Ice Shapes on Airfoils: Experimental Investigation", AIAA Paper No. 99-0092, Reno, NV, January 11-14, 1999.

[2] Brumby, R.E., "Wing Surface Roughness - Cause and Effect," *D.C. Flight Approach*, Jan. 1979, pp. 2-7.

[3] Jacobs, E.N., "Airfoil Section Characteristics as Affected by Protuberances," NACA Report No. 446, 1932.

[4] Hoerner, S.F, *Fluid-Dynamic Lift*, Hoerner Fluid Dynamics, Brick Town, NJ, 1975, p4-19.

[5] Morgan, H.L., Ferris, J.C., and McGhee, R.J., "A Study of High-Lift Airfoils at High Reynolds Number in Langley Low-Turbulence Pressure Tunnel," NASA TM-89125, July 1987.

[6] Kim, H.S. and Bragg, M.B., "Effect of Leading Edge Ice Accretion on Airfoil Performance," AIAA Paper 99-3150, 17th Applied Aerodynamics Conference, Norfolk, VA, June 28-July 1, 1999.

[7] Lee, S., Kim, H., and Bragg, M. B., "Investigation of Factors that Influence Iced-Airfoil Aerodynamics", AIAA Paper No. 2000-0099, Reno, NV, January 10-13, 2000.

[8] Lee, S. and Bragg, M.B., "An Experimental Investigation of Simulated Large-Droplet Ice Shapes on Airfoil Aerodynamics," *Journal of Aircraft*, Vol. 36, No. 5, Sept-Oct. 1999, pp. 844-850.

[9] Lee, S., Dunn, T., Gurbacki, H.M., Bragg, M.B., and Loth, E., "An Experimental and Computational Investigation of Spanwise-Step-Ice Shapes on Airfoil Aerodynamics," AIAA Paper 98-0490, 36th Aerospace Sciences Meeting & Exhibit, Reno, NV 1998.

[10] Rae, W. H. and Pope, A., *Low-Speed Wind Tunnel Testing*, John Wiley & Sons, 1984.

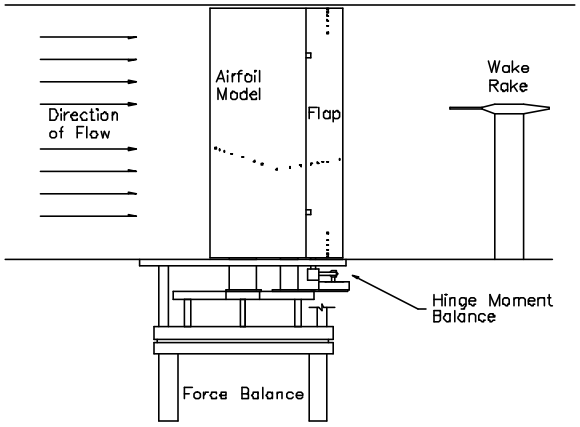

Fig. 1: University of Illinois experimental setup.

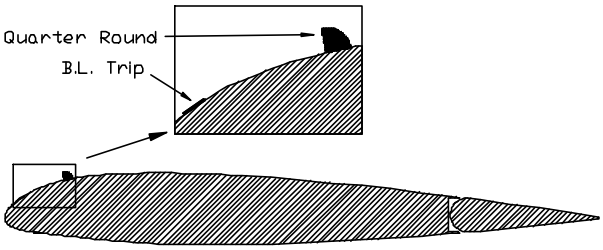

Fig. 2: NACA 23012m airfoil and spanwise protuberance geometry.

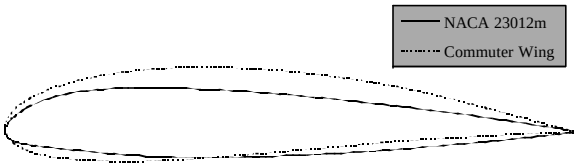

Fig. 3a) NACA 23012m and Commuter wing

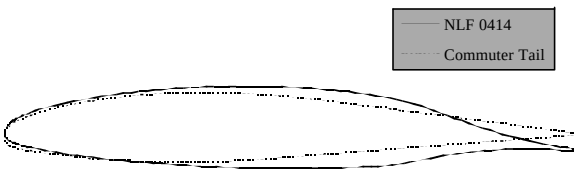

Fig. 3b) NLF 0414 and Commuter tail

Fig. 3: Geometry comparison of four airfoils tested at Illinois.

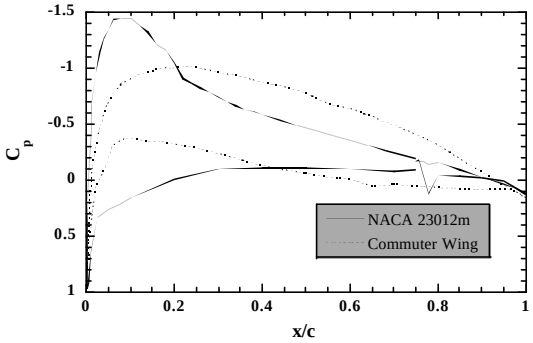

Fig. 4a) NACA 23012m (α = 4.12°) and commuter wing (α = 1.02°)

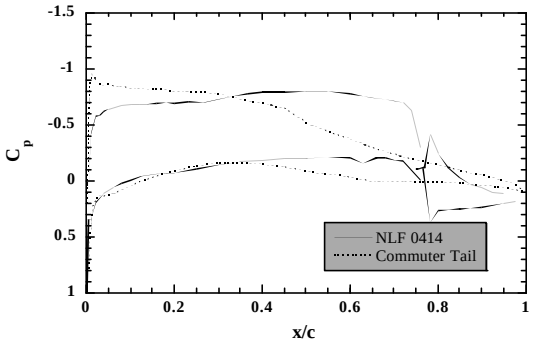

Fig. 4b) NLF 0414 (α = 0.02°) and commuter tail (α = 3.07°)

Fig. 4: Clean-model surface pressure comparison. C_l = 0.5

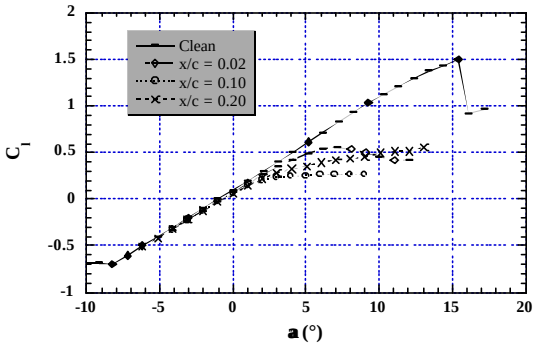

Fig. 5a) NACA 23012m

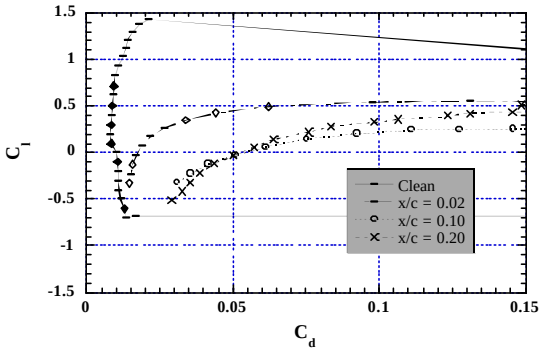

Fig. 6a) NACA 23012m

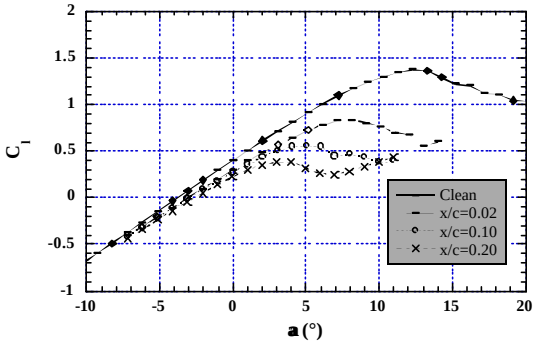

Fig. 5b) Commuter wing

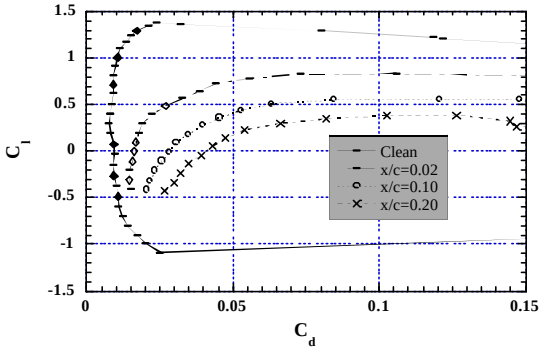

Fig. 6b) Commuter wing

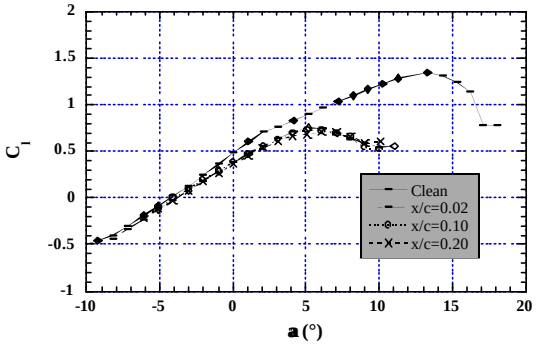

Fig. 5c) NLF 0414

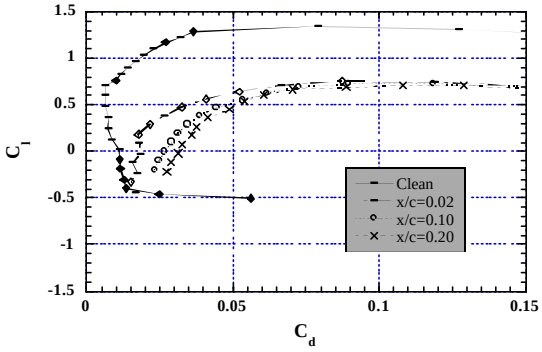

Fig. 6c) NLF 0414

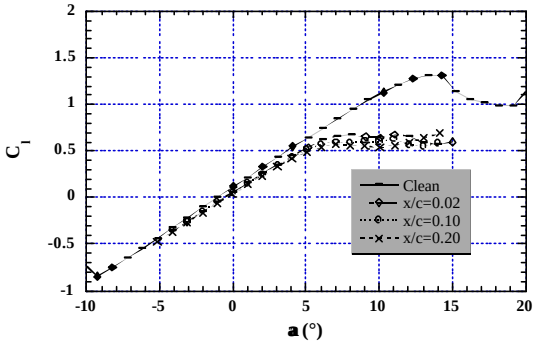

Fig. 5d) Commuter tail

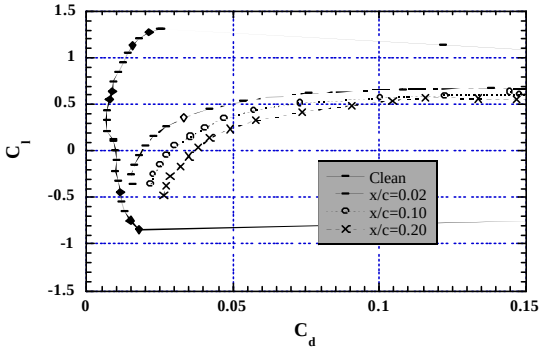

Fig. 6d) Commuter tail

Fig. 5: Effect ice ridge-ice location on lift. Re = 1.8 million.

Fig. 6: Effect of ridge-ice location on drag. Re = 1.8 million.

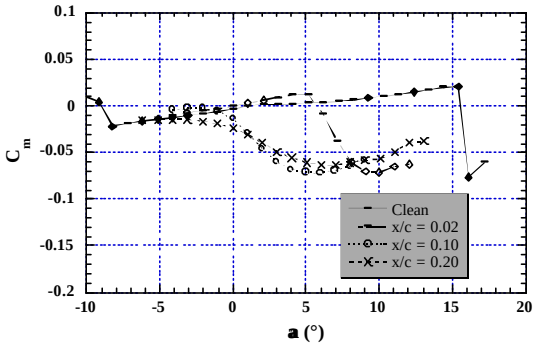

Fig. 7a) NACA 23012m

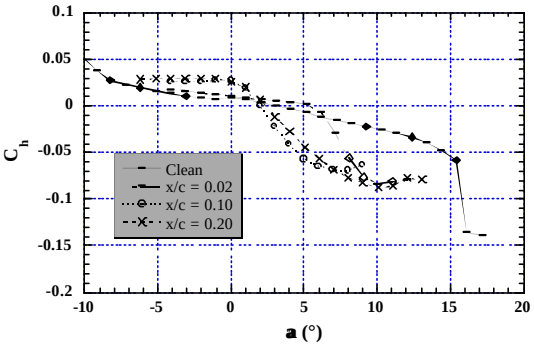

Fig. 8a) NACA 23012m

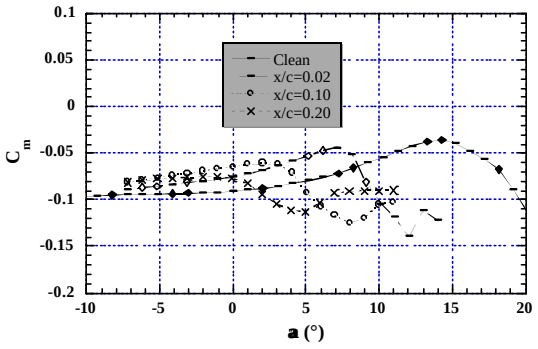

Fig. 7b) Commuter wing

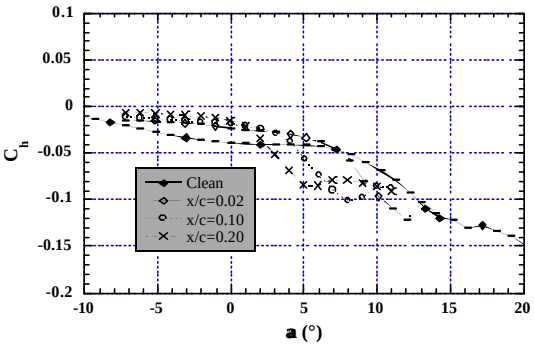

Fig. 8b) Commuter wing

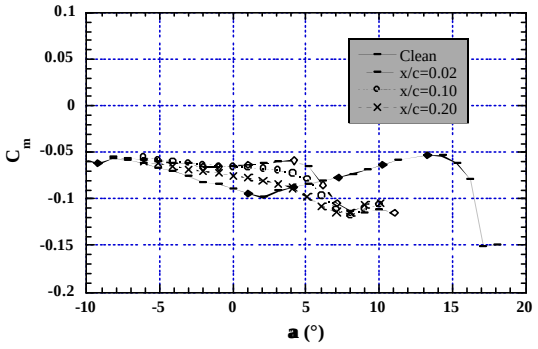

Fig. 7c) NLF 0414

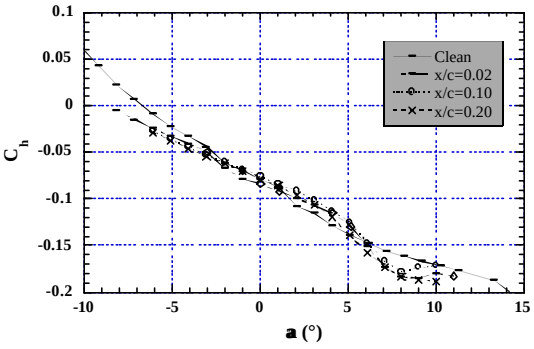

Fig. 8c) NLF 0414

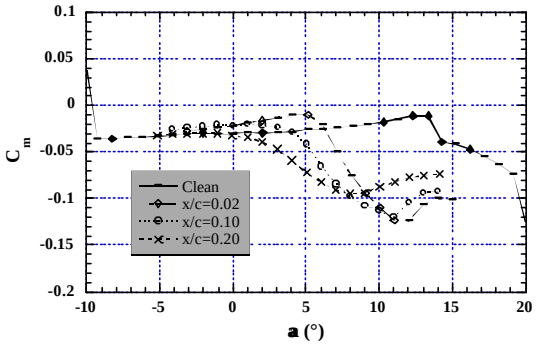

Fig. 7d) Commuter tail

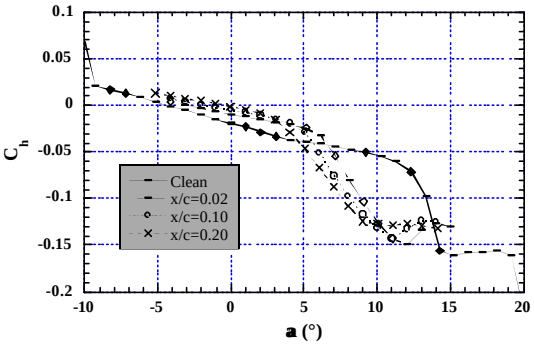

Fig. 8d) Commuter tail

Fig. 7: Effect of ridge-ice location on pitching moment. Re = 1.8 million.

Fig. 8: Effect of ridge-ice location on flap-hinge moment. Re = 1.8 million.

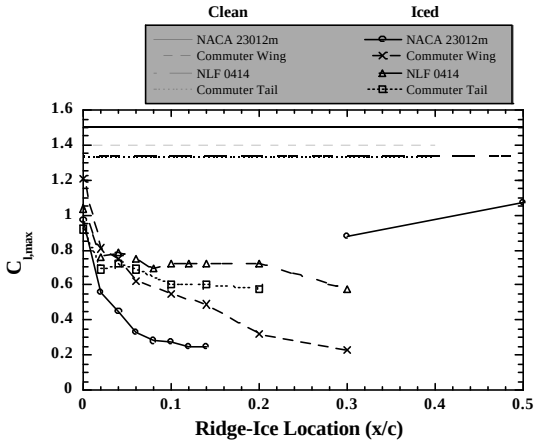

Fig. 9: Effect of ridge-ice location on maximum lift. Re = 1.8 million.

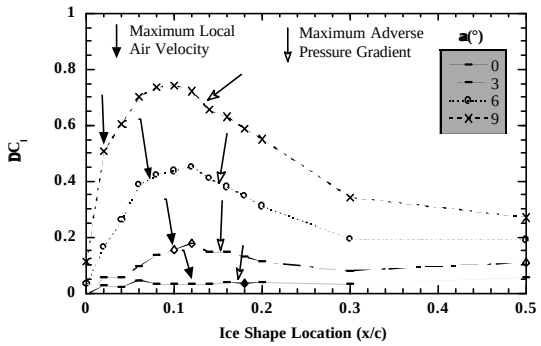

Fig. 10a) NACA 23012m

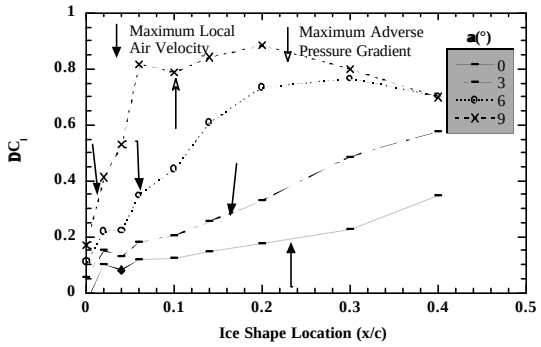

Fig. 10b) Commuter wing

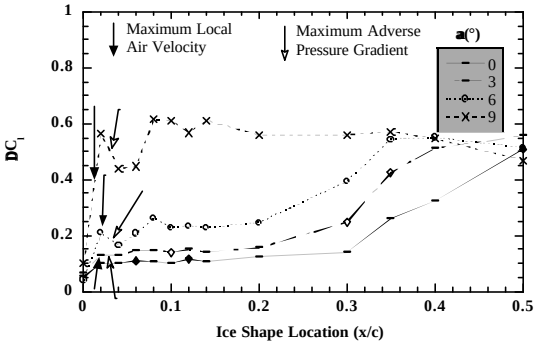

Fig. 10c) NLF 0414

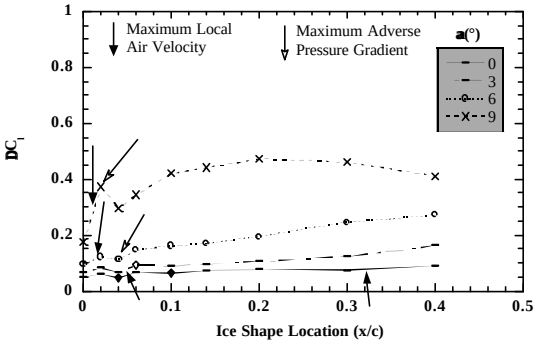

Fig. 10d) Commuter tail

Fig. 10: Effect of ridge-ice location on lift loss. Re = 1.8×10^6.

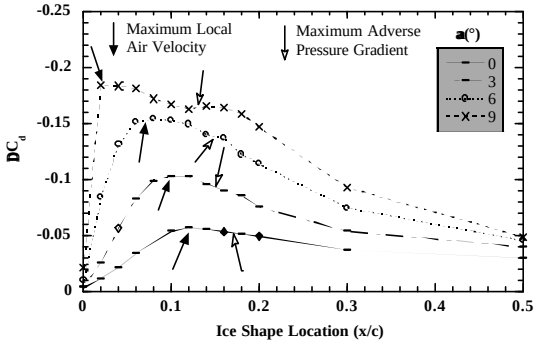

Fig. 11a) NACA 23012m

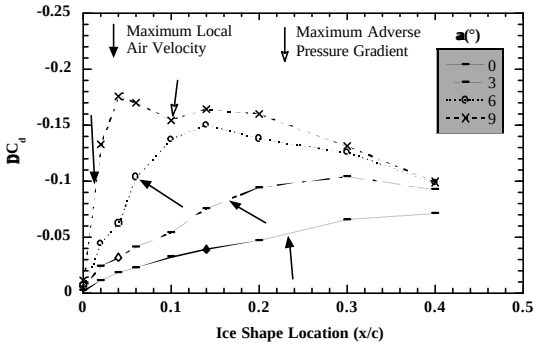

Fig. 11b) Commuter wing

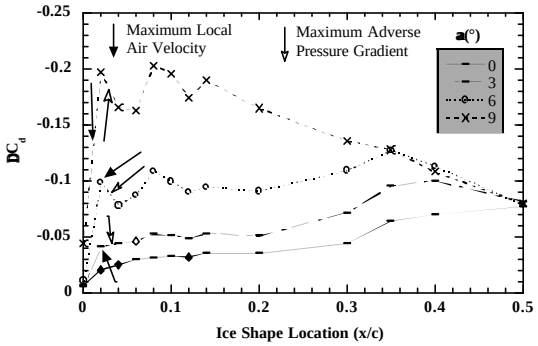

Fig. 11c) NLF 0414

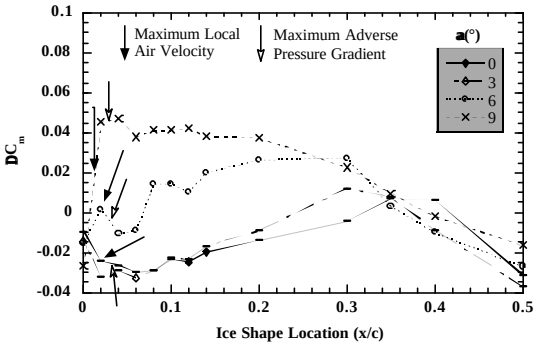

Fig. 12c) NLF 0414

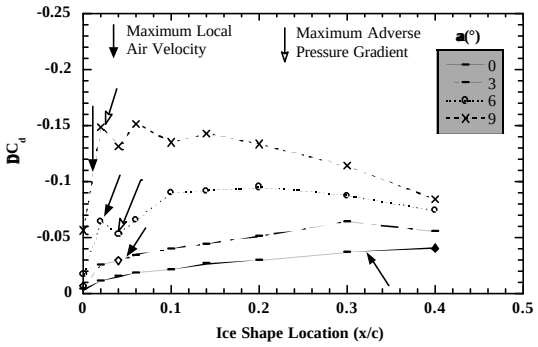

Fig. 11d) Commuter tail

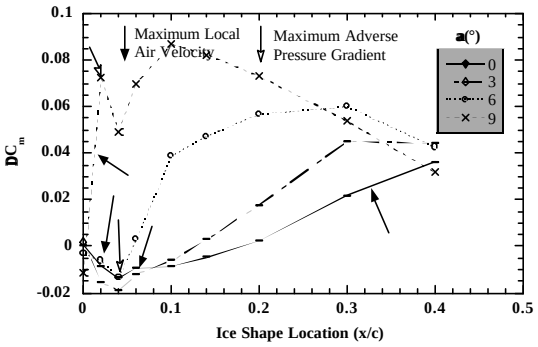

Fig. 12d) Commuter tail

Fig. 11: Effect of ridge-ice location on drag increase. Re = 1.8×10^6.

Fig. 12: Effect of ridge-ice location on pitching moment. Re = 1.8×10^6.

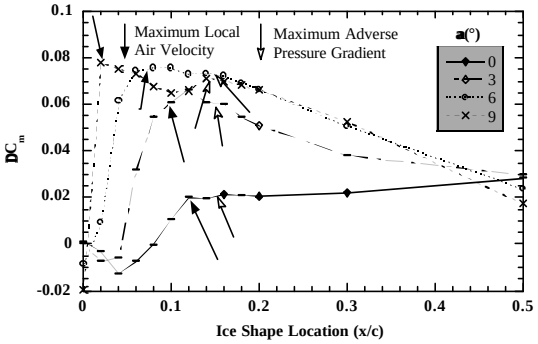

Fig. 12a) NACA 23012

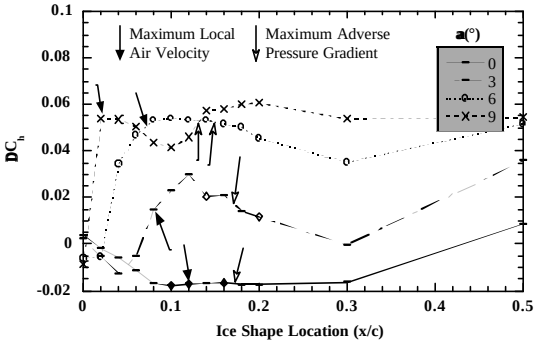

Fig. 13a) NACA 23012m

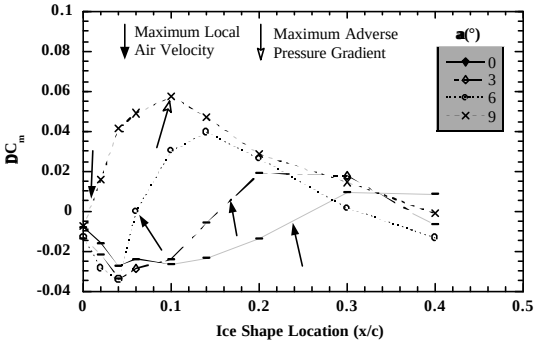

Fig. 12b) Commuter wing

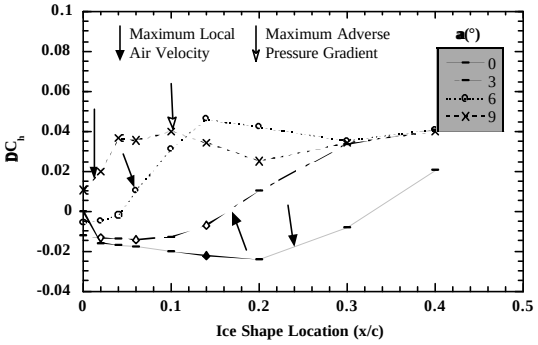

Fig. 13b) Commuter wing

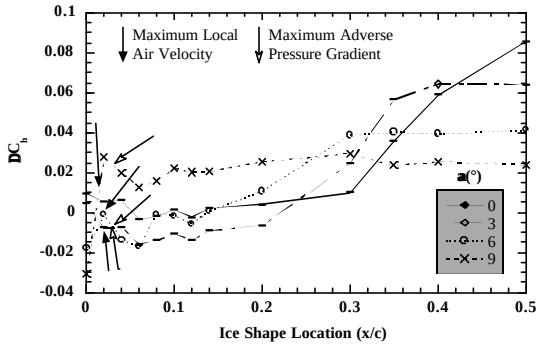

Fig. 13c) NLF 0414

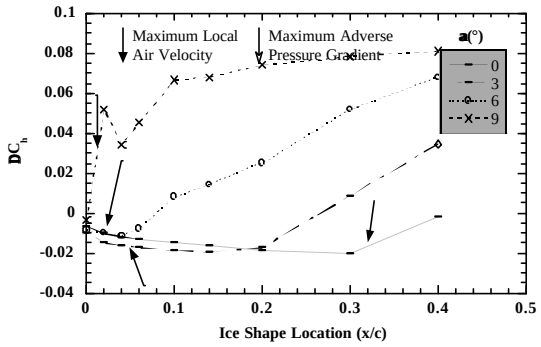

Fig. 13d) Commuter tail

Fig. 13: Effect of ridge-ice location on hinge moment. Re = 1.8×10^6.

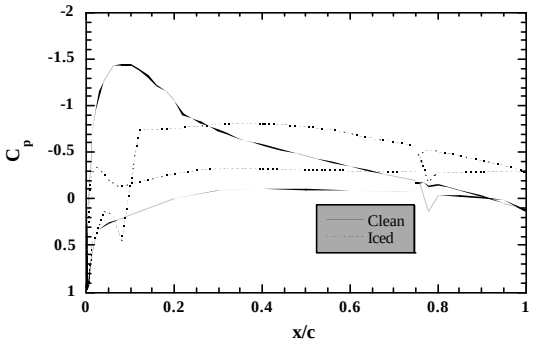

Fig. 14a) NACA 23012m ($\alpha = 4°$)

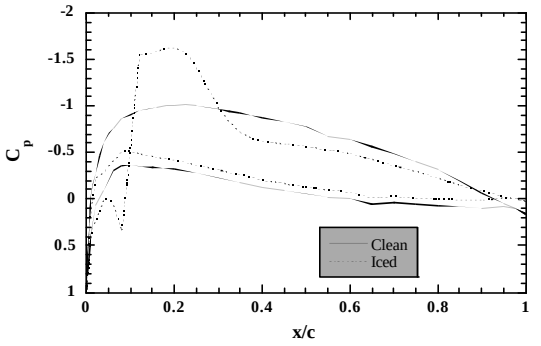

Fig. 14b) Commuter wing ($\alpha = 1°$)

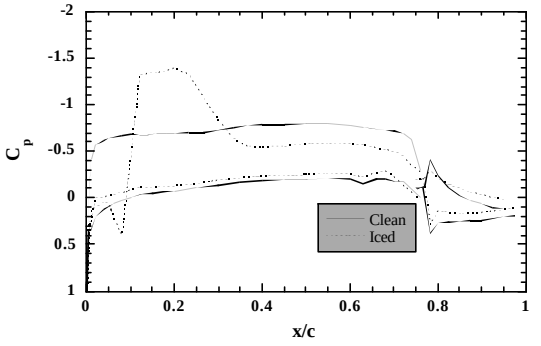

Fig. 14c) NLF 0414 ($\alpha = 0°$)

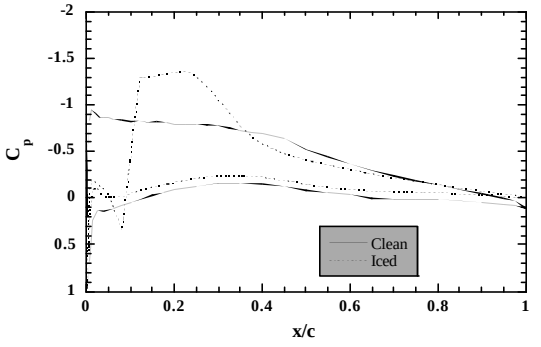

Fig. 14d) Commuter tail ($\alpha = 3°$)

Fig. 14: Effect of ridge ice on surface pressure distribution. Ridge ice at x/c = 0.10. Re = 1.8 million. Clean model $C_l = 0.5$.